ACS central science

http://pubs.acs.org/journal/acscii

Article

Open Access

This article is licensed under CC-BY 4.0

# Protein-Controlled Photochemical Redirection Enables Proximity-Activated Red-Light Photocatalytic Pharmacology

Ru He,[#] Qihang Zhao,[#] Zikang Chen, Xiuyu Wang, Qiaoling Che, Kaixing Zeng, Yi Zeng,* Yixin Zhang,* and Yiyun Chen*

Cite This: https://doi.org/10.1021/acscentsci.6c01125

Read Online

ACCESS | Metrics & More | Article Recommendations | Supporting Information

**ABSTRACT:** Red-light photocatalysis offers opportunities for noninvasive molecular regulation but is challenged by competing pathways that generate cytotoxic reactive oxygen species. Here, we report a protein-controlled photochemical redirection strategy for proximity-activated red-light photocatalytic pharmacology through bioorthogonal deboronative hydroxylation. By integrating a silicon rhodamine (SiR) photocatalyst with a HaloTag scaffold, we establish a protein–photocatalyst hybrid that stabilizes and confines the photoactive open zwitterionic SiR state. Mechanistic studies associate a higher open-state population with preferential Type I photochemical reactivity, supporting superoxide radical anion generation and downstream hydrogen peroxide formation while strongly suppressing singlet oxygen production ($\Phi_\Delta$ = 0.0027). This enables efficient deboronative hydroxylation with yields exceeding 99% and high cellular compatibility. The genetically targetable platform enables proximity-activated pharmacological regulation in living cells. Nuclear-localized release of an HDAC inhibitor increased histone H3 lysine 9 acetylation (H3K9ac) to 2.9 times the control level, compared with 1.9 times the control level following nonlocalized activation under identical conditions, demonstrating that pharmacological outcomes depend on the subcellular site of photocatalytic activation. Photocatalytic activity was also retained through a 1.5 mm tissue barrier under attenuated illumination. These findings establish protein-mediated stabilization and confinement of a photoactive chromophore as a strategy for controlling red-light photochemical reactivity and enabling proximity-activated photocatalytic pharmacology in living systems.

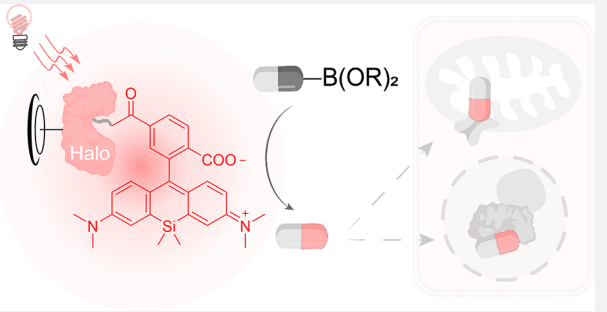


## INTRODUCTION

Light-mediated regulation provides a uniquely powerful strategy for interrogating biological processes with exceptional spatiotemporal precision and minimal invasiveness.[1−5] Among available optical modalities, red light ($\lambda$ > 600 nm) is particularly attractive because of its superior tissue penetration and reduced interference from endogenous chromophores, offering an ideal window for noninvasive chemical control in complex biological systems.[6−8] Despite these advantages, the broader application of red-light photochemistry remains fundamentally constrained by a persistent challenge: low-energy excitation is frequently accompanied by inefficient chemical transformations[9] and competing reactive oxygen species (ROS) pathways[10] that limit both reaction efficiency and biocompatibility.

Red-light photoredox catalysis, enabled by both transition-metal complexes and organic dyes, provides an attractive solution by decoupling photon absorption from chemical bond activation through catalytic turnover.[11−13] However, translating photoredox catalysis into living systems requires simultaneously maximizing catalytic efficiency while minimizing cytotoxic ROS generation.[14−16] In particular, many red-light photosensitizers predominantly generate singlet oxygen ($^1O_2$) through Type II energy transfer.[17] Because $^1O_2$ can indiscriminately oxidize biomolecules, these chromophores have consequently been used primarily for destructive applications such as photodynamic therapy and cell ablation.[18−22] Moving red-light photocatalysis from destructive photochemistry toward molecular regulation therefore requires not only new chromophores but also strategies to control the photochemical reaction pathway itself (Figure 1A).

Silicon rhodamine (SiR) dyes have emerged as promising red-light chromophores owing to their high molar absorptivity, biocompatibility, and tunable photochemical properties.[23] Recent studies have repurposed SiR fluorophores for red-light bioorthogonal activation in living systems (Table S1).[24−27] However, controlling photocatalytic reactivity in

Received: June 29, 2026
Revised: October 12, 2026
Accepted: October 14, 2026

ACS Publications

© XXXX The Authors. Published by American Chemical Society



Downloaded from pubs.acs.org/acscii/article-pdf/doi/10.1021/acscentsci.6c01125/6907009/acscentsci.6c01125.pdf by SHANGHAI INST OF ORGANIC CHEMISTRY, Yiyun Chen on 04 November 2026

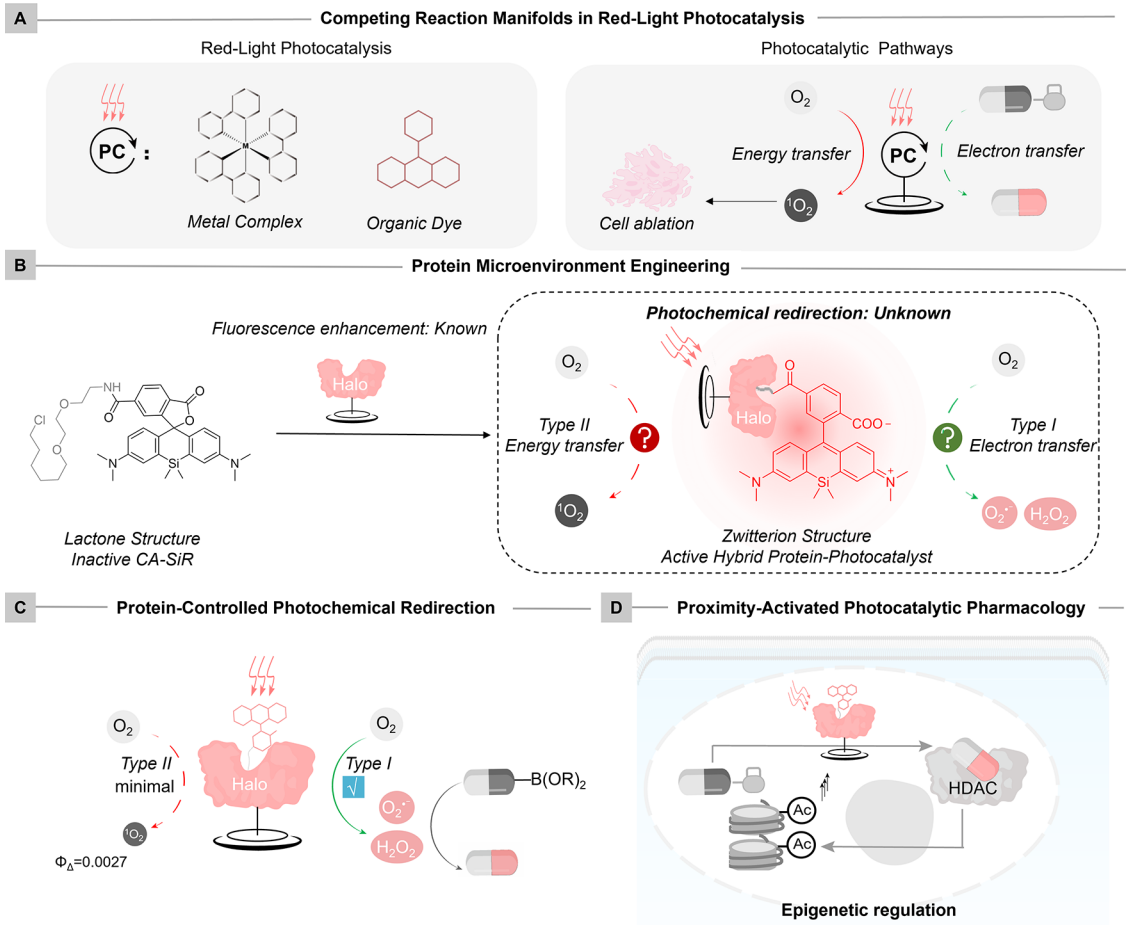


**Figure 1.** Protein-controlled photochemical redirection enables proximity-activated red-light photocatalytic pharmacology. (A) Competing reaction manifolds in red-light photocatalysis. Conventional photosensitizers predominantly undergo Type II energy transfer to generate cytotoxic singlet oxygen ($^1O_2$), restricting their use to destructive photochemistry. Redirecting excited-state reactivity toward a Type I electron-transfer pathway enables biocompatible molecular regulation. (B) Protein microenvironment engineering. HaloTag functions as an active protein microenvironment that constrains SiR conformation and stabilizes its catalytically competent zwitterionic state, establishing a protein-controlled photocatalyst. (C) Protein-controlled photochemical redirection. The engineered protein microenvironment reshapes oxygen activation by suppressing Type II photosensitization while favoring a biocompatible Type I electron-transfer pathway, thereby enabling efficient deboronative hydroxylation with minimal singlet oxygen generation. (D) Proximity-activated photocatalytic pharmacology. Genetic targeting directs the protein-photocatalyst hybrid assembly to specific subcellular compartments, enabling proximity-activated bioorthogonal activation and demonstrating that the site of photocatalysis directly determines pharmacological outcome.

biological environments remains challenging, particularly when competing ROS-generating pathways can compromise cellular compatibility.[26,27] We reasoned that controlling the chromophore's conformational state and local environment could provide an alternative means of influencing photocatalytic reactivity.

Nature provides a compelling precedent for protein-mediated control of photochemical behavior.[28−30] In particular, Johnsson and co-workers showed that HaloTag binding shifts the spirocyclization equilibrium of SiR toward its photoactive, open zwitterionic state, thereby enhancing fluorescence.[31−33] Although protein scaffolds are widely used to control molecular reactivity and photophysics,[34,35] their potential to regulate photocatalytic reaction pathways remains largely unexplored. We therefore envisioned that the protein-mediated stabilization and confinement of the open SiR state could influence its photocatalytic reactivity, potentially favoring Type I over Type II photochemistry under biologically compatible conditions (Figure 1B).

Among bioorthogonal transformations,[36−41] deboronative hydroxylation is particularly attractive for biological applications because organoboronates[42−44] offer high chemoselectivity, metabolic stability, and broad compatibility with biological systems. Although deboronative hydroxylation has been used for hydrogen peroxide sensing[45] and photocatalytic organic synthesis,[46] its application as a bioorthogonal reaction for photocatalytic drug uncaging in living systems represents a distinct advance. Our previous studies established blue-light-driven proximity-activated photocatalytic pharmacology using organic dyes, hybrid photoenzymes, and the genetically encoded Type I photocatalyst miniSOG for bioorthogonal boronate uncaging.[47−49] Together, these studies laid the foundation for proximity-activated photocatalytic pharmacology, which we have since extended from subcellular compartments to neural circuits.[50] However, blue-light excitation limits tissue penetration, and the flavin cofactor undergoes photobleaching under prolonged irradiation.[51] To address these limitations, we sought to develop a red-light-responsive protein−photocatalyst hybrid by integrating silicon rhodamine


https://doi.org/10.1021/acscentsci.6c01125
ACS Cent. Sci. XXXX, XXX, XXX−XXX

Downloaded from pubs.acs.org/acscii/article-pdf/doi/10.1021/acscentsci.6c01125/6907094/acscentsci.6c01125.pdf by SHANGHAI INST OF ORGANIC CHEMISTRY, Yiyun Chen on 04 November 2026

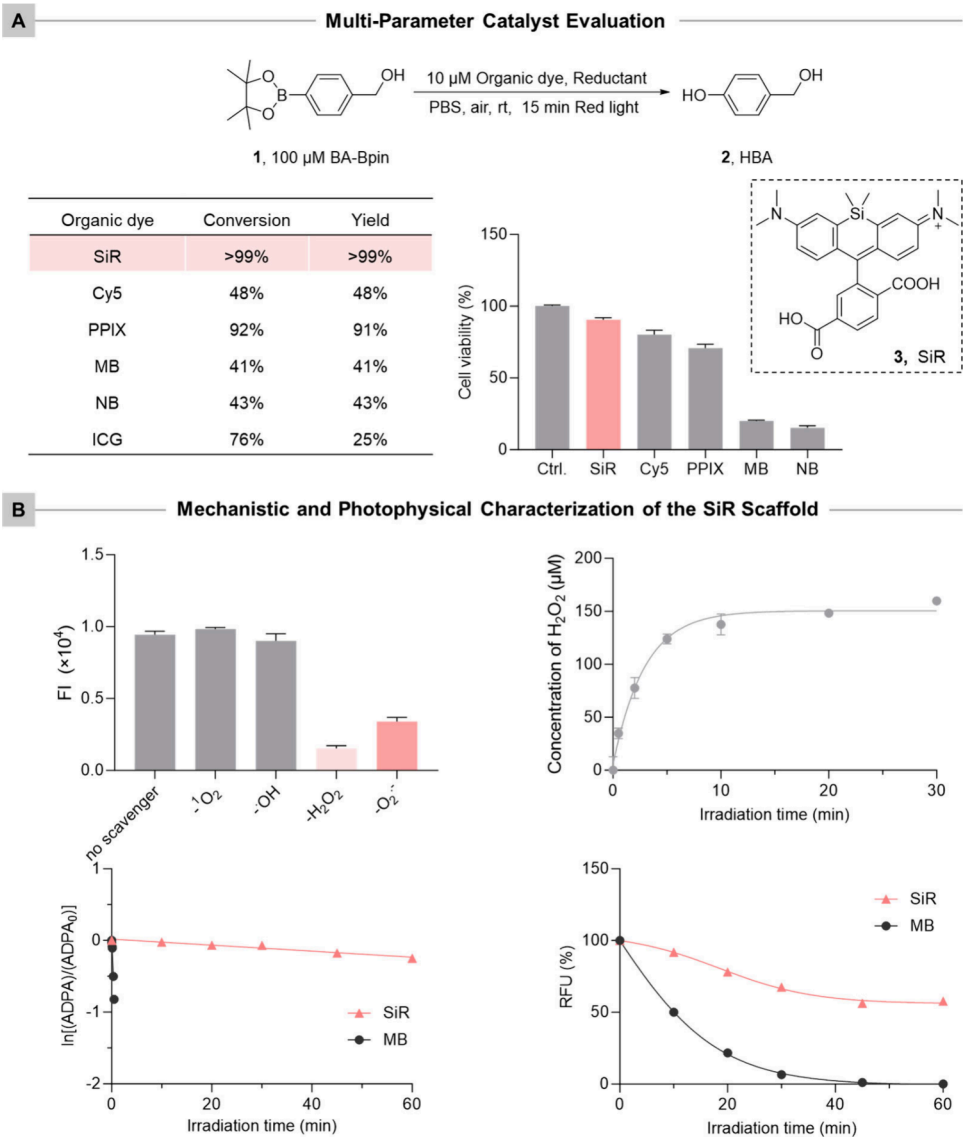


**Figure 2.** Identification of a biocompatible SiR scaffold for red-light photocatalytic deboronative hydroxylation. (A) Multiparameter catalyst evaluation. Left: Comparative screening of diverse organic fluorophores for the deboronative hydroxylation of **1**. Right: Corresponding cytocompatibility profiles in HEK 293T cells. SiR (**3**) exhibits a favorable balance of catalytic turnover and low phototoxicity. (B) Mechanistic and photophysical characterization of the SiR scaffold. Top left: Identification of reactive oxygen species (ROS) via chemical quenching; the predominance of $O_2^{\bullet-}$ and $H_2O_2$ is consistent with a Type I photocatalytic cycle. FI: fluorescence intensity of AMC released from AMC-Bpin. Top right: Real-time quantification of $H_2O_2$ production. Bottom left: Quantitative determination of $^1O_2$ generation via ADPA bleaching; SiR exhibits negligible $^1O_2$ generation compared with MB. ADPA: absorbance of anthracene-9,10-dipropionic acid at 400 nm. Bottom right: Photostability assays under sustained red-light irradiation (635 nm). RFU: relative fluorescence units. The fluorescence intensity of the group without light irradiation was defined as 100%. Data represent mean ± SEM ($n$ = 3 independent experiments).

(SiR) with a genetically targetable HaloTag scaffold.[52] We hypothesized that this architecture could stabilize and confine the photoactive zwitterionic SiR state while providing a distinct local reaction environment, thereby favoring Type I photochemical reactivity and enabling efficient, cytocompatible red-light-driven bioorthogonal deboronative hydroxylation (Figure 1C).

Here, we report a genetically encoded Halo−SiR protein−photocatalyst hybrid that enables protein-mediated photochemical redirection for proximity-activated red-light photocatalytic pharmacology (Figure 1D). By combining protein-mediated stabilization and confinement of the photoactive SiR state with genetically encoded subcellular targeting, the platform achieves near-quantitative bioorthogonal deboronative hydroxylation (>99%) and spatially controlled release of bioactive molecules. Nuclear-localized HDAC inhibitor activation produced a 2.9-fold increase in H3K9 acetylation, compared with 1.9-fold for nonlocalized activation under identical conditions, demonstrating that the site of photocatalytic activation influences pharmacological outcome. This strategy provides a complementary approach to chromophore-centered photochemical design and enables spatially controlled red-light photocatalysis in living cells.


https://doi.org/10.1021/acscentsci.6c01125
ACS Cent. Sci. XXXX, XXX, XXX−XXX

Downloaded from pubs.acs.org/acscii/article-pdf/doi/10.1021/acscentsci.6c01125/6907009/acscentsci.6c01125.pdf by SHANGHAI INST OF ORGANIC CHEMISTRY, Yiyun Chen on 04 November 2026

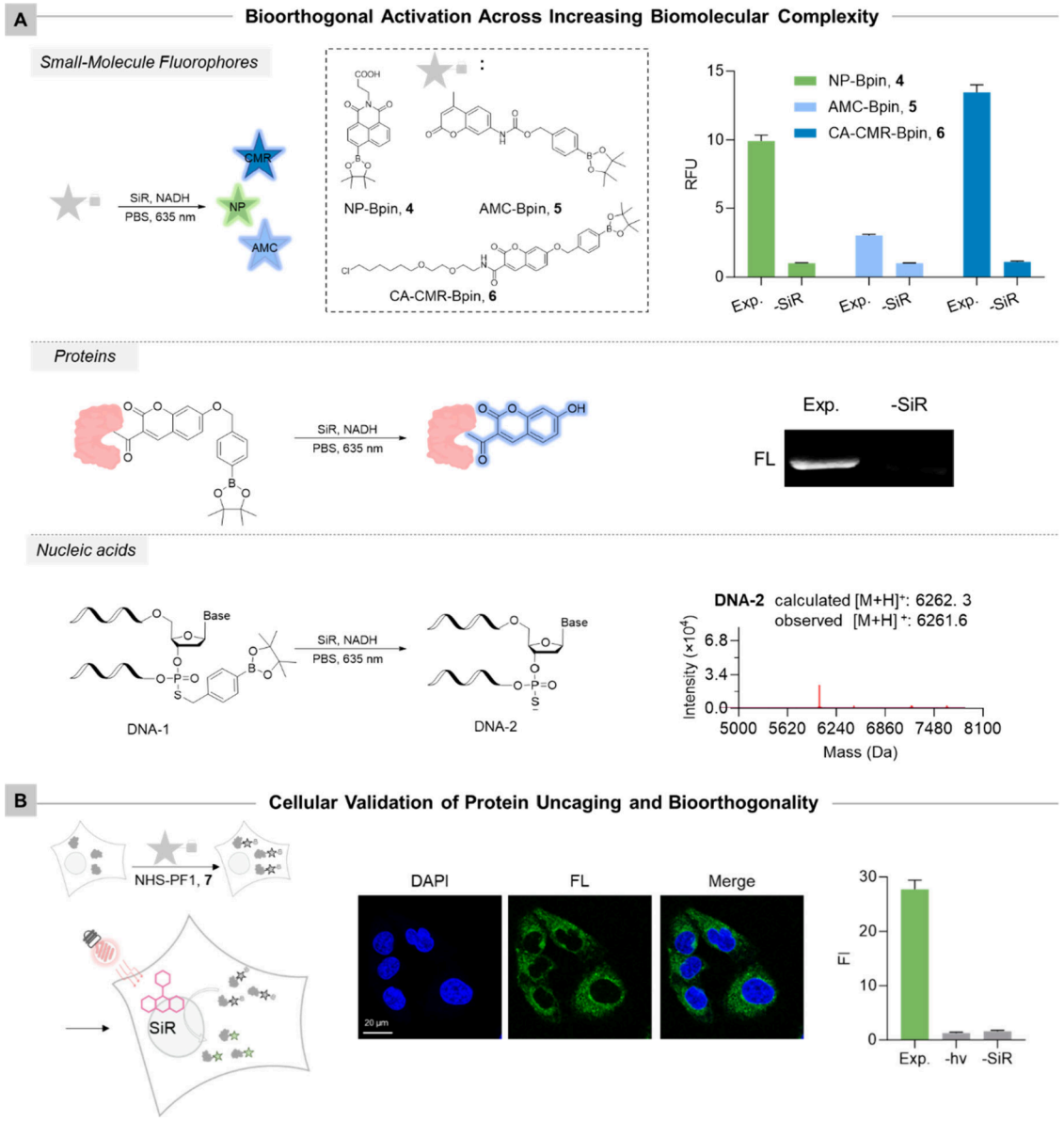


**Figure 3.** Broad biomolecular compatibility of red-light photocatalytic deboronative hydroxylation. (A) Bioorthogonal activation across increasing biomolecular complexity. Top: Red-light photocatalysis of blue- and green-emitting fluorophores (100 $\mu$M caged fluorophores) using SiR (10 $\mu$M) and NADH (1 mM) under red-light irradiation (635 nm, 40 mW cm$^{-2}$, 15 min), demonstrating spectral orthogonality. RFU: relative fluorescence units. The fluorescence intensity of the group without SiR was defined as 1.0. Data represent mean ± SEM ($n$ = 3). Middle: Site-specific activation of a boronate-caged protein (Halo-CMR-Bpin, 10 $\mu$M) using SiR (10 $\mu$M), analyzed by SDS-PAGE and gel fluorescence imaging. Bottom: Photocatalytic activation of a boronate-caged oligonucleotide (DNA-1, 50 $\mu$M) using SiR (50 $\mu$M) and NADH (5 mM), with conversion confirmed by mass spectrometry. (B) Cellular validation of protein uncaging and bioorthogonality. Establishing that the SiR photocatalytic manifold remains effective across diverse biomolecular architectures provided the foundation for subsequently investigating how protein microenvironment engineering can further reshape its photocatalytic behavior. Confocal microscopy of HeLa cells shows red-light-triggered activation of a cellular protein labeled with NHS-PF1 (7, 50 $\mu$M) using SiR (5 $\mu$M) and NADH (5 mM) (635 nm, 70 mW cm$^{-2}$, 15 min). High signal-to-noise ratios and absence of dark activation confirm strict photodependence in a complex cellular environment. FI: Average fluorescein (FL) fluorescence intensity of individual cells quantified via ImageJ software. Data represent mean ± SEM ($n$ = 5 cells per group). Scale bars: 20 $\mu$m.

## RESULTS

### Red-Light-Driven Photocatalytic Deboronative Hydroxylation via a Biocompatible SiR System

To identify a biocompatible red-light photocatalytic platform suitable for protein-controlled photochemical redirection, we performed a multiparameter screening of diverse photocatalyst classes based on their absorption properties, catalytic activity, and cellular compatibility.[53] To assess the structural scope of chromophores compatible with this photoredox chemistry, we screened 19 chromophores spanning six major structural classes: silicon rhodamines, classical rhodamines/xanthenes, BODIPYs, cyanines, porphyrins/phthalocyanines, and phenothiazines/oxazines (Figures S1 and S2). Using a model deboronative hydroxylation reaction under red-light irradiation (635 nm, 40 mW cm$^{-2}$, 15 min), silicon rhodamine (SiR, **3**) emerged as the most suitable scaffold, affording near-quantitative conversions (>99%, Figure 2A, left). MTT assays


https://doi.org/10.1021/acscentsci.6c01125
ACS Cent. Sci. XXXX, XXX, XXX−XXX

Downloaded from pubs.acs.org/acscii/article-pdf/doi/10.1021/acscentsci.6c01125/6907009/acscentsci.6c01125.pdf by SHANGHAI INST OF ORGANIC CHEMISTRY, Yiyun Chen on 04 November 2026

in HEK293T cells further showed that SiR exhibited high cytocompatibility, with >90% cell viability following incubation with 2 $\mu$M dye and irradiation at 635 nm (130 mW cm$^{-2}$, 15 min). In contrast, other efficient photocatalysts, including MB, NB, and PPIX, caused substantially greater cytotoxicity under identical conditions, with cell viability ranging from <20% to 70% (Figure 2A, right).[54]

The combination of high catalytic efficiency, cytocompatibility, and favorable photophysical properties led us to select SiR as the scaffold for the subsequent protein microenvironment engineering. The SiR-mediated reaction operates through a three-component photocatalytic system comprising SiR, NADH, and light. Control experiments confirmed that all three components were required for efficient reaction, with the complete system affording >99% substrate conversion and product yield, whereas omission of any single component reduced reactivity to <1% (Figure S3).

Organoboron caging groups are particularly well suited for this platform because their oxidative activation proceeds efficiently under ambient oxygen, tolerates biological reductants, and generates benign byproducts. These features distinguish organoboronates from nitrobenzyl-[27] and azobenzene-based[13] photocaging systems, which often require higher photon flux or generate cytotoxic intermediates under red-light conditions. Guided by recent reports of red-light-driven NADH oxidation by silicon rhodamine dyes,[55] we evaluated physiologically relevant reducing equivalents as potential redox partners. Both NADH and NADPH supported quantitative (>99%) conversion of BA-Bpin under red-light irradiation (Figure S4A), demonstrating that either reduced pyridine nucleotide can efficiently support the proposed Type I photocatalytic cycle. The contribution of NADH to the reaction was further examined by real-time monitoring, which revealed rapid and substantial NADH consumption (~35% depletion within 60 min; Figure S4C). The photocatalytic transformation was readily tuned by catalyst loading and irradiation intensity, with measurable conversion observed even at low catalyst concentration (1 $\mu$M) or low photon flux (8 mW cm$^{-2}$) (Figure S4D,E).

Mechanistic studies reveal that free SiR exhibits predominantly Type I photochemical reactivity under our experimental conditions, with minimal singlet oxygen generation, providing a favorable baseline for subsequent protein-mediated photochemical control. Scavenger experiments identified $O_2^{\bullet-}$ and $H_2O_2$ as the dominant ROS, with their respective quenching reducing catalytic yield to 36% and 16% of control levels (Figure 2B, top left panel). This ROS partitioning is well suited to bioorthogonal deboronative hydroxylation while minimizing oxidative damage to surrounding biomolecules. The SiR system exhibited high catalytic efficiency, generating a cumulative $O_2^{\bullet-}/H_2O_2$ flux approaching 150 $\mu$M from only 10 $\mu$M catalyst within 15 min of red-light irradiation (Figure 2B, top right panel; Figure S5). Quantitative detection revealed that SiR generates negligible $^1O_2$ ($\Phi_\Delta$ = 0.0012), a value over 400-fold lower than MB ($\Phi_\Delta$ = 0.5) (Figure 2B, bottom left panel).[56]

This exceptionally low $^1O_2$ generation is consistent with reduced oxidative stress toward sensitive biomolecules, including DNA and proteins, which remained undamaged under operational light doses (Figure S6A,B). Furthermore, SiR exhibited good photostability, retaining ~ 92% of its initial fluorescence after 10 min of illumination and maintaining ~58% after 60 min. This represents a > 50-fold greater retention than MB (Figure 2B, bottom right panel; Figure S6C,D), enabling simultaneous catalysis and real-time fluorescence tracking. Together with the excellent physiological stability of BA-Bpin **1** (Figure S7), these properties establish SiR as a robust biocompatible scaffold for subsequent protein-mediated photochemical control in complex biological environments.

## Broad Bioorthogonal Compatibility Across Increasing Levels of Biomolecular Complexity

To establish the generality and bioorthogonality of the SiR photocatalytic manifold prior to protein microenvironment engineering, we evaluated its compatibility across chemically and structurally diverse biomolecular architectures. We first examined spectral orthogonality in deboronative hydroxylation (Figure S8). As shown in Figure 3A (top panel), the platform efficiently uncages both green-emitting (NP-Bpin **4**) and blue-emitting (AMC-Bpin **5**, CA-CMR-Bpin **6**) fluorophores under red-light irradiation. Red light excitation preserves the orthogonality of shorter-wavelength fluorophores, effectively decoupling photocatalytic activation from fluorescence visualization and enabling simultaneous photocatalysis and optical readout.

We next challenged the photocatalytic manifold with increasingly complex biomolecular architectures, progressing from small molecules to proteins and oligonucleotides, to determine whether catalytic efficiency could be maintained in sterically and structurally demanding environments.[25,57] A coumarin-caged protein conjugate (Halo-CMR-Bpin) exhibited a robust fluorescence increase upon red light irradiation (Figure 3A, middle panel), consistent with efficient photocatalytic activation within a protein-conjugated biomolecular environment. Similarly, red-light-driven activation of a boronate-caged oligonucleotide proceeded with high conversion, as verified by mass spectrometry (Figure 3A, bottom panel; Figure S9).

Finally, we evaluated whether the broad biomolecular compatibility observed in vitro could be translated to the intracellular environment. Red-light irradiation of HeLa cells containing SiR, NADH, and a cellular protein labeled with boronate-caged fluorophore NHS-PF1 (**7**) resulted in a rapid fluorescence increase due to SiR-catalyzed deboronative hydroxylation (Figure 3B; Figure S10).[58,59] Light-dependent intracellular AMC release from boronate-caged **5** (AMC-Bpin) was further validated in HeLa cells (Figure S14). Under severe hypoxia (1% $O_2$), intracellular uncaging was maintained, while cell-free reactions afforded >99% conversion after 15 min under both normoxic and hypoxic conditions (Figures S11 and S12). Under TNF-$\alpha$-induced inflammatory stress, which elevated intracellular ROS, negligible AMC release was observed in the dark, whereas red-light irradiation triggered robust uncaging (Figures S13 and S14), supporting the light dependence and selectivity of boronate activation under the tested conditions.

Collectively, these results establish that the SiR photocatalytic manifold is intrinsically compatible with biomolecular complexity, enabling high-fidelity bioorthogonal activation across small molecules, proteins, nucleic acids, and living cells. This broad substrate compatibility provides the molecular foundation for the protein-controlled photochemical redirection described in the following section.

Downloaded from pubs.acs.org/acscii/article-pdf/doi/10.1021/acscentsci.6c01125/6907094/acscentsci.6c01125.pdf by SHANGHAI INST OF ORGANIC CHEMISTRY, Yiyun Chen on 04 November 2026


https://doi.org/10.1021/acscentsci.6c01125
ACS Cent. Sci. XXXX, XXX, XXX−XXX

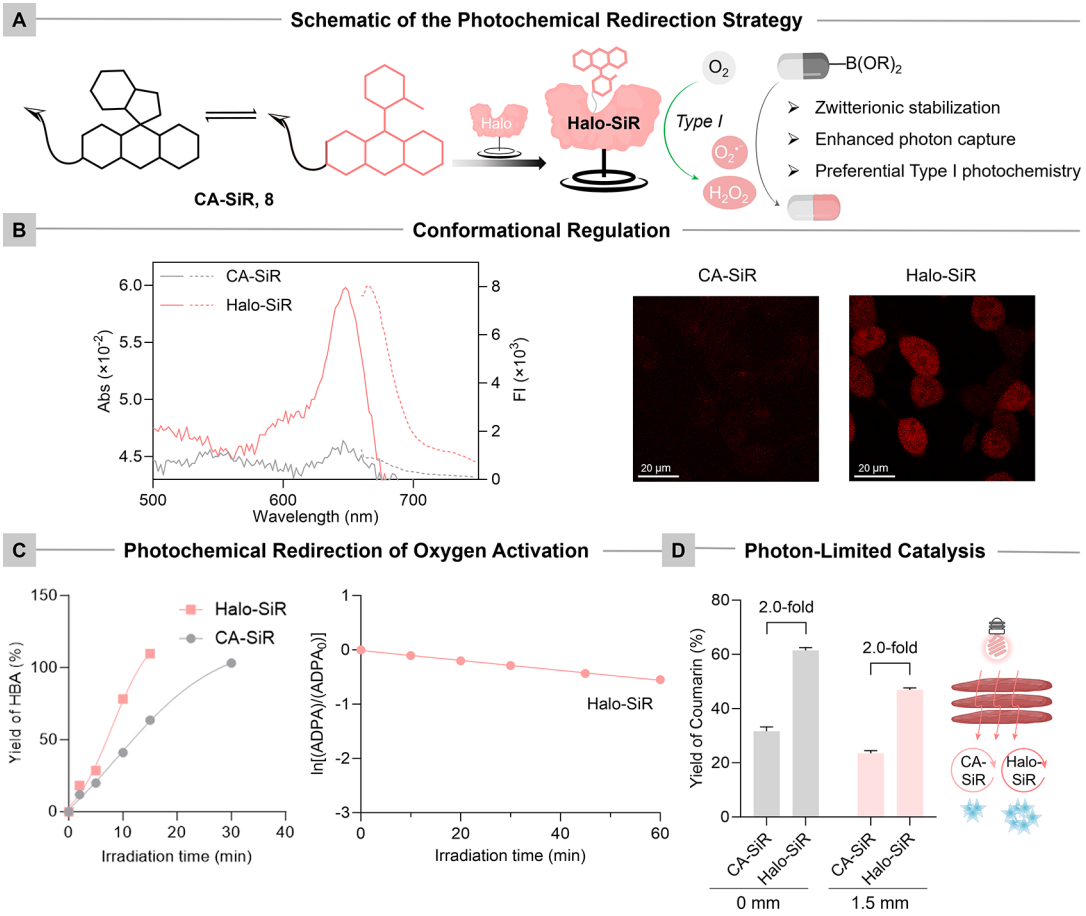


**Figure 4.** Protein-mediated control of SiR photochemistry favors Type I oxygen activation. (A) Schematic of the photochemical redirection strategy: site-specific conjugation of the SiR ligand to the HaloTag protein stabilizes the catalytically active ring-opened zwitterionic isomer. (B) Conformational regulation. Left: Absorption spectra and emission spectra of Halo-SiR versus free ligand CA-SiR (**8**), demonstrating a significant enhancement in molar extinction coefficient within the red-light therapeutic window. Right: Live-cell confocal imaging confirming the superior brightness and intracellular stability of the Halo−SiR hybrid photocatalyst compared to nontargeted **8**. Abs: Absorbance. (C) Photochemical redirection of oxygen activation. Left: Halo-SiR exhibits significantly elevated catalytic performance for deboronative hydroxylation of **1** relative to the free ligand CA-SiR (**8**), consistent with a protein-induced transition toward a Type I electron-transfer pathway. Middle: Quantitative determination of $^1O_2$ generation via ADPA bleaching; Halo-SiR exhibits substantially lower $^1O_2$ flux ($\Phi_\Delta$= 0.0027) compared to MB. (D) Photon-limited catalysis: Comparative catalytic efficiency under attenuated photon flux (1.5 mm ex vivo raw beef). Halo-SiR maintains efficient photocatalysis (>40% activation), representing a 2-fold enhancement over the free ligand **8**. Yields were determined using a 7-boronate coumarin reporter (20 $\mu$M) in PBS buffer (10 mM, pH 7.4) with 1 mM NADH and 1 $\mu$M photocatalyst. Irradiation: 635 nm red LEDs (70 mW cm$^{-2}$) for 15 min. Yield (%) = 100 × ($FI_{15\ min}$−$FI_{0\ min}$) /$FI_{H2O2}$, where $FI_{H2O2}$ is the fluorescence of the reporter fully reacted with 2 mM $H_2O_2$.

## Protein Microenvironment Engineering Redirects Red-Light Photocatalytic Reactivity

To determine whether protein microenvironment engineering can influence photocatalytic reactivity, we constructed a genetically encoded Halo-SiR hybrid photocatalyst by integrating HaloTag with its cell-permeable SiR ligand, CA-SiR (**8**) (Figure 4A).[23,60] The formation of the Halo-SiR complex was confirmed by SDS-PAGE (Figure S15A). Spectroscopic analysis demonstrated that HaloTag binding promotes ring opening of SiR, resulting in a pronounced electronic turn-on effect: the assembled Halo-SiR complex exhibited a 7.8-fold increase in absorptivity and a 9.3-fold enhancement in fluorescence compared to the free CA-SiR (**8**) (Figure 4B, left panel; Figure S15B). Consistent with previous studies, HaloTag functions as a conformational constraint that shifts the spirocyclization equilibrium toward the photochemically competent zwitterionic state.[61] To gain insights into the HaloTag-associated microenvironment of SiR, we constructed a template-derived covalent HaloTag9-SiR model based on the crystal structure of HaloTag-TMR (PDB 6ZVY).[62] The open SiR adduct could be geometrically accommodated within the HaloTag-associated environment without substantial steric clashes, with partial, model-dependent solvent shielding of the chromophore predicted by the model (Figure S16 and Table S2).[63]

These improvements translated directly to the cellular environment; live-cell confocal imaging revealed markedly higher intracellular fluorescent brightness (Figure 4B, right panel). We next asked whether the photocatalytic performance of Halo-SiR could be maintained under an attenuated photon flux characteristic of optically challenging biological environments. We assessed the catalytic efficiency of Halo-SiR and free CA-SiR using a fluorogenic 7-boronate coumarin reporter in both the presence and absence of an *ex vivo* tissue barrier (Figure S15C). Halo-SiR achieved approximately 2.0-fold higher coumarin release than free CA-SiR, both in open solution (62% vs 32%) and behind a 1.5 mm-thick ex vivo tissue barrier (raw beef) used for quantitative attenuation


https://doi.org/10.1021/acscentsci.6c01125
ACS Cent. Sci. XXXX, XXX, XXX−XXX

Downloaded from pubs.acs.org/acscii/article-pdf/doi/10.1021/acscentsci.6c01125/6907094/acscentsci.6c01125.pdf by SHANGHAI INST OF ORGANIC CHEMISTRY, Yiyun Chen on 04 November 2026

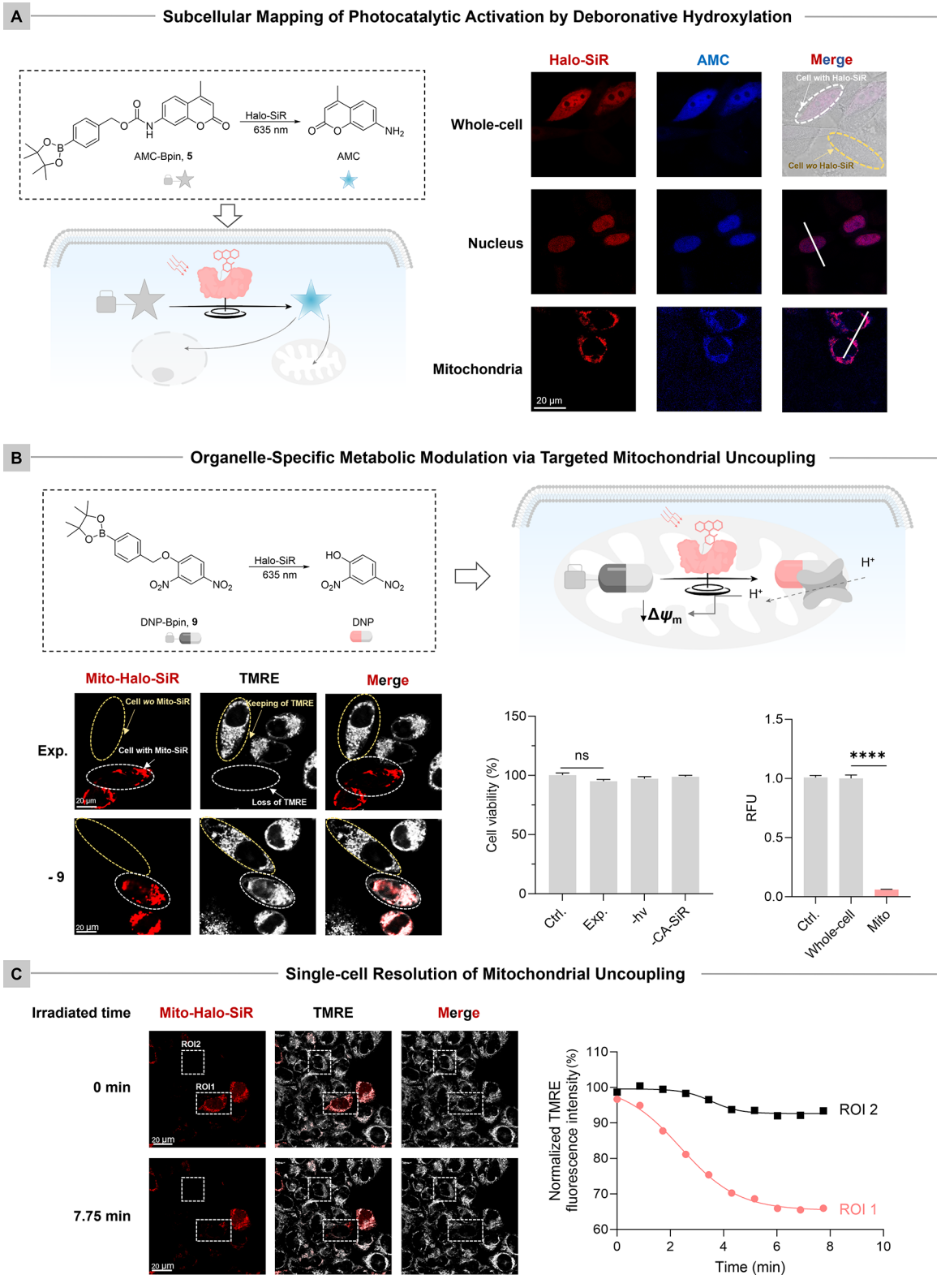


**Figure 5.** Proximity-activated photocatalytic pharmacology enables organelle-specific regulation. (A) Subcellular mapping of photocatalytic activation by deboronative hydroxylation. Genetic targeting of the Halo−SiR hybrid photocatalyst to the nucleus (NLS-Halo-SiR, red) or mitochondria (Mito-Halo-SiR, red) facilitates site-specific uncaging of the fluorogenic reporter AMC-Bpin (**5**, 100 $\mu$M, blue) after red-light irradiation (635 nm, 130 mW cm$^{-2}$, 60 min). Confocal microscopy (right) shows that the uncaging signal is predominantly localized to the targeted organelle, demonstrating organelle-confined fluorophore liberation. Scale bars: 20 $\mu$m. (B) Organelle-specific metabolic modulation via targeted mitochondrial uncoupling. Red-light irradiation triggers the proximity-activated liberation of DNP, resulting in the rapid dissipation of the mitochondrial membrane potential ($\Delta\psi_m$), as quantified by loss of mitochondrial TMRE sequestration (1 $\mu$M, gray). Bottom left: Representative confocal images of HeLa cells expressing Mito-Halo-SiR (red), treated with the caged uncoupler DNP-Bpin (**9**) and red-light irradiation (635 nm, 130 mW cm$^{-2}$, 10 min). Bottom middle: MTT assays confirming the high cytocompatibility and safety of the targeted photocatalytic treatment



https://doi.org/10.1021/acscentsci.6c01125
ACS Cent. Sci. XXXX, XXX, XXX−XXX

Downloaded from pubs.acs.org/acscii/article-pdf/doi/10.1021/acscentsci.6c01125/6907009/acscentsci.6c01125.pdf by SHANGHAI INST OF ORGANIC CHEMISTRY, Yiyun Chen on 04 November 2026

**Figure** 5. continued

(635 nm, 130 mW $cm^{-2}$, 30 min). Ctrl. represents the DMSO-only group, which was set as 100%. Data represent mean ± SEM ($n$ = 5). Bottom right: Spatial control validation demonstrating that whole-cell-Halo-SiR fails to induce depolarization under identical conditions. This disparity demonstrates that biological outcome is determined by the subcellular site of photocatalytic activation rather than total cellular catalyst loading or photon dose. RFU: relative fluorescence units. Mean cellular TMRE fluorescence intensities were quantified using ImageJ software and normalized relative to the DMSO-only control group (Ctrl., set to 1.0). Scale bars: 20 $\mu$m. Data represent mean ± SEM ($n$ = 5 cells per group). ****$p$ < 0.0001 by two-tailed Student's $t$-test; ns = not significant. (C) Single-cell spatiotemporal control of photocatalytic mitochondrial uncoupling. HeLa cells expressing Mito-HaloTag were coincubated with CA-SiR (0.5 $\mu$M), DNP-Bpin (100 $\mu$M), and TMRE (1 $\mu$M) for 1 h to label the photocatalyst and monitor mitochondrial membrane potential ($\Delta\psi$m). A single Mito-HaloTag-positive cell was selectively irradiated at 633 nm using a confocal FRAP module (100% nominal laser power, 30 s per cycle, 10 cycles; 300 s total irradiation), while time-lapse images were acquired throughout the experiment (total observation period, 7.75 min). Proximity-activated photocatalytic uncaging of DNP-Bpin induced a selective loss of TMRE fluorescence in the targeted Mito-HaloTag-positive cell (ROI 1), whereas an adjacent Mito-HaloTag-negative cell (ROI 2) retained robust TMRE fluorescence. Time-lapse quantification of TMRE fluorescence intensity across irradiation cycles is shown in the right panel. Complete dynamic recordings are provided in Supplementary Movie S1.

validation (47% vs 24%; Figure 4D). Introducing a biological scattering barrier between the light source and the reaction solution therefore provides a quantitative model of photon-limited conditions encountered in optically dense biological environments.

To experimentally examine the relationship between the open SiR population and photochemical reactivity, we performed solvent-tuning experiments at constant total SiR concentration. Increasing Abs635, used as a proxy for the open SiR population, was associated with increased superoxide generation and a higher $O_2^{\bullet-}/^1O_2$ ratio (Figure S17), supporting a link between the open SiR state and preferential Type I photochemical reactivity under the conditions examined.

We next examined whether this protein-mediated stabilization and confinement of the open SiR state could be associated with enhanced photocatalytic reactivity. The Halo−SiR hybrid exhibited substantially enhanced catalytic deboronative hydroxylation activity, achieving quantitative conversion of BA-Bpin (**1**) within 15 min and significantly outperforming the free CA-SiR ligand (Figure 4C, left panel).[64] Quantitative ROS profiling revealed a distinct oxygen-reactivity profile for Halo−SiR, characterized by enhanced O2•−/$H_2O_2$-associated signals. This profile is consistent with preferential Type I electron-transfer chemistry under the conditions examined. The resulting Halo-SiR complex exhibits an exceptionally low $^1O_2$ quantum yield at 0.0027 (Figure 4C, middle panel)—substantially lower than established photoenzymatic benchmarks such as miniSOG ($\Phi_\Delta$= 0.03).[49]

Femtosecond transient-absorption spectroscopy following 635 nm excitation revealed excited-state absorption near 430 nm and ground-state bleaching near 652 nm. Addition of NADH accelerated the apparent decay of the Halo−SiR transients, supporting an NADH-dependent perturbation of the excited-state population dynamics (Figure S21A−E). EPR spin-trapping experiments under red-light irradiation further detected a 1:2:2:1 quartet assigned to a DMPO−OH-type oxygen-centered radical adduct, consistent with downstream radical ROS formation (Figure S21F).[65] Prolonged irradiation revealed that Halo-SiR exhibits greater photostability than CA-SiR in 0.1% SDS at comparable absorbance at 635 nm (Figure S20). Notably, Halo−SiR retained measurable photocatalytic activity in the absence of added NADH or NADPH, affording 6% product yield compared with negligible activity for free CA−SiR (Figure S22A). NADH titration further showed that substantial activity was maintained at low exogenous NADH concentrations, while higher NADH concentrations enhanced the reaction (Figure S22B), supporting a role for NADH in promoting photocatalytic turnover without assigning the residual activity to a specific protein electron donor.

Importantly, the protein scaffold does not alter the tissue transparency or the intrinsic penetration depth of red light. Rather, its performance advantage under attenuated illumination is consistent with the stabilization and confinement of the catalytically competent zwitterionic state, which increases the effective population of the absorbing species and thereby enhances photon capture. Overall, these findings support protein-mediated stabilization and confinement of the photoactive SiR state as a strategy for sustaining efficient and biocompatible red-light photocatalysis under photon-limited biological conditions while providing a complementary means of controlling photocatalytic reactivity through the protein-associated microenvironment.

## Proximity-Activated Photocatalytic Pharmacology Enables Organelle-Specific Regulation

We next investigated whether genetically encoded localization could spatially localize photocatalytic activity with single organelle precision. The scaffold-bound SiR catalyst drives the red-light-induced uncaging of the fluorogenic substrate AMC-Bpin to release fluorescent AMC, enabling real-time monitoring of local catalytic turnover and spatial localization; HPLC confirmed clean AMC formation (Figure S23). In HeLa cells expressing a diffuse variant of Halo-SiR (whole-cell-Halo-SiR, lacking organelle-targeting sequences), a robust AMC signal was selectively detected within Halo-SiR-positive cells, whereas nonexpressing control cells exhibited no detectable background fluorescence (Figure 5A, top panel). This result demonstrates that genetically encoded catalyst localization is sufficient to localize the photocatalytic activity at the single-cell level. To achieve subcellular resolution, Halo-SiR was targeted to either the nucleus (NLS-Halo-SiR) or the mitochondria (Mito-Halo-SiR), both of which demonstrated precise colocalization with their respective organelle markers (Figure S24A). Finally, we evaluated the photocytocompatibility of the platform via propidium iodide (PI) staining; cells subjected to the standard red light irradiation protocol exhibited negligible cell death (Figure S24B), supporting the cytocompatibility of this scaffold-directed architecture.

Upon incubation with AMC-Bpin **5** (100 $\mu$M), red-light irradiation generated fluorescent AMC predominantly at the genetically targeted organelle. In cells expressing NLS-Halo-SiR, the uncaging signal was predominantly localized to the nucleus, whereas cells expressing Mito-Halo-SiR exhibited preferential fluorescence within mitochondria (Figure 5A,


https://doi.org/10.1021/acscentsci.6c01125
ACS Cent. Sci. XXXX, XXX, XXX−XXX

Downloaded from pubs.acs.org/acscii/article-pdf/doi/10.1021/acscentsci.6c01125/6907094/acscentsci.6c01125.pdf by SHANGHAI INST OF ORGANIC CHEMISTRY, Yiyun Chen on 04 November 2026

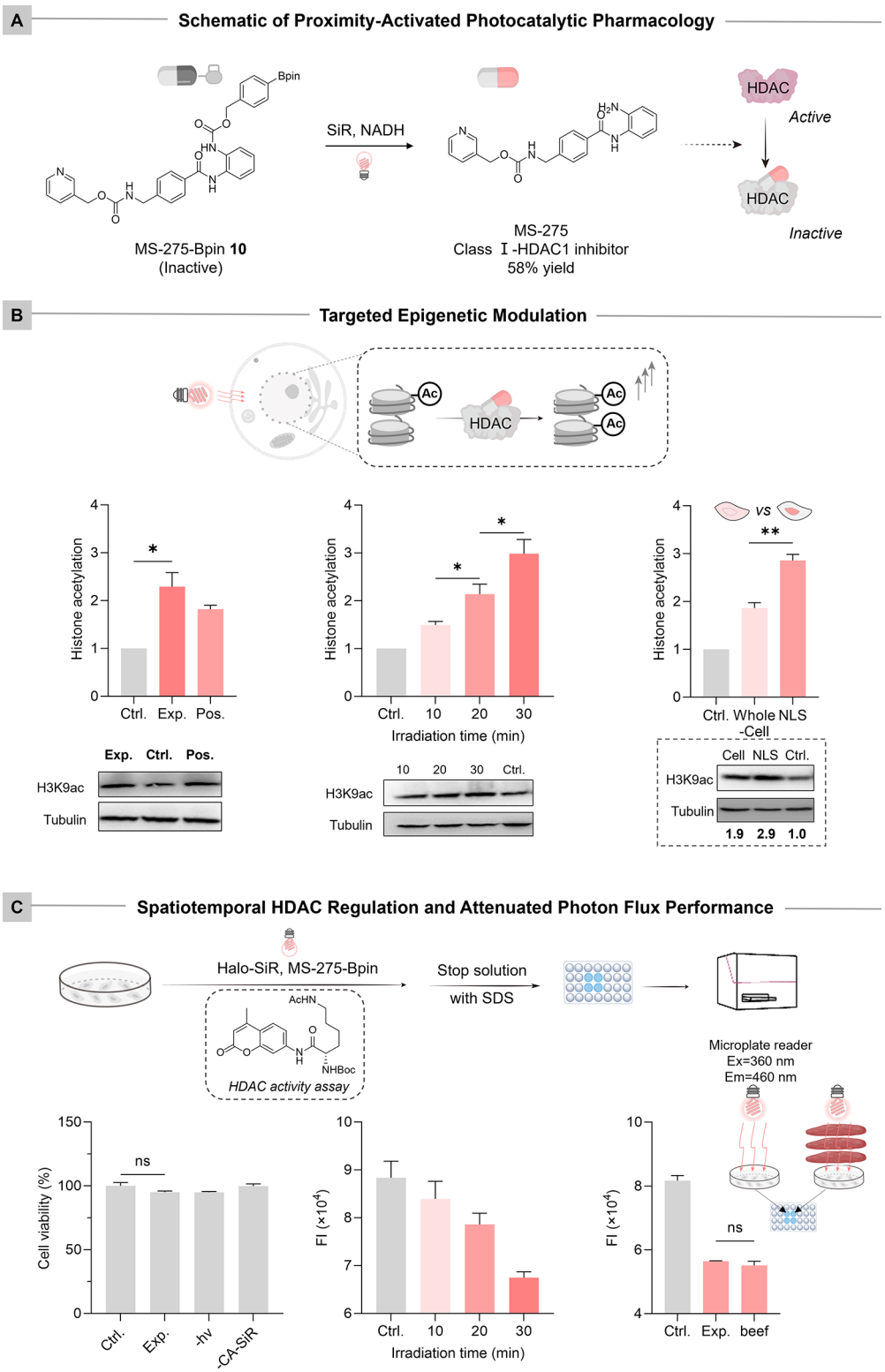


**Figure 6.** Nuclear-targeted photocatalysis enables proximity-activated HDAC inhibition and epigenetic modulation. (A) Schematic of the proximity-activated photocatalytic pharmacology: the SiR photocatalyst facilitates the red-light-driven deboronative hydroxylation of the inert prodrug **10**, liberating the potent histone deacetylase (HDAC) inhibitor MS-275 directly within the nuclear compartment. (B) Targeted epigenetic modulation. The platform exhibits high reaction efficacy in live cells (left), temporal tunability via dose-dependent irradiation (middle), and a clear spatial advantage, where nuclear-targeted activation (NLS-Halo-SiR) significantly outperforms nontargeted, whole-cell catalysis (whole-cell-Halo-SiR, right). Comparison of nuclear-targeted and globally distributed photocatalysis reveals a pronounced spatial efficacy gap, where proximity-activated inhibitor generation at the chromatin interface produces substantially stronger epigenetic responses under identical irradiation conditions. The normalized H3K9Ac/tubulin ratio for the DMSO-treated control group was set to 1.0. All experimental values are expressed as the fold change relative to this control. Data represent mean ± SEM ($n$ = 3 independent biological replicates). (C) Spatiotemporal HDAC regulation and attenuated photon flux performance. Left: MTT assays confirming the high cytocompatibility of the photocatalytic treatment. Ctrl represents the


https://doi.org/10.1021/acscentsci.6c01125
ACS Cent. Sci. XXXX, XXX, XXX−XXX

Downloaded from pubs.acs.org/acscii/article-pdf/doi/10.1021/acscentsci.6c01125/6907094/acscentsci.6c01125.pdf by SHANGHAI INST OF ORGANIC CHEMISTRY, Yiyun Chen on 04 November 2026

**Figure** 6. continued

DMSO-only group, which was normalized to 100%. Data represent mean ± SEM ($n$ = 5 independent biological replicates). Middle: Fluorescence-based quantification of uncaging kinetics, demonstrating rapid and efficient payload release (FI: fluorescence intensity of AMC released by active HDACs). Right: Performance under biological shielding, where photocatalytic activation remains effective through a 1.5 mm-thick tissue barrier, demonstrating robust operation under biologically relevant light attenuation. Data represent mean ± SEM ($n$ = 3 independent biological replicates). Significance: *$p$ < 0.05, **$p$ < 0.01 by two-tailed Student's $t$ test; ns = not statistically significant.

middle and bottom panels).[66] Line-profile analysis confirmed spatial coincidence between the Halo-SiR catalyst and the liberated fluorophore (Figure S26A). In contrast, no detectable AMC fluorescence was observed in dark controls (Figure S26B), demonstrating strict light dependence with negligible background activation. Together, these results support Halo-SiR as a genetically programmable photocatalyst capable of directing bioorthogonal deboronative hydroxylation with high subcellular precision. Light-dependent AMC-Bpin uncaging persisted without exogenous NADH and after FK866 pretreatment, indicating that cellular reducing equivalents can support light-dependent uncaging under these conditions (Figure S27).[67]

Having established subcellularly proximity-activated photocatalysis, we next asked a more fundamental question: does the subcellular site of photocatalysis determine pharmacological outcome? We applied it to modulate mitochondrial membrane potential ($\Delta\psi_m$), a central regulator of cellular metabolism.[68] The mitochondrial uncoupler 2,4-dinitrophenol (DNP) is a potent metabolic regulator whose clinical application is precluded by systemic toxicity arising from nonselective distribution.[69] We therefore hypothesized that Mito-Halo-SiR could enable localized DNP activation at mitochondria, thereby generating a proximity-activated pharmacological response that is inaccessible to globally distributed activation (Figure 5B, top panel).

Initial *in vitro* assays confirmed that red-light irradiation of the SiR/NADH system efficiently uncaged DNP from the boronate-caged prodrug DNP-Bpin (**9**), reaching a 59% yield within 5 min (Figure S28). We next asked whether genetically localized photocatalysis could translate this chemical transformation into organelle-specific biological regulation. In HeLa cells expressing Mito-Halo-SiR, 10 min of red-light irradiation triggered a loss of mitochondrial membrane potential ($\Delta\psi_m$), as visualized by a > 90% dissipation of the voltage-sensitive dye TMRE (Figure 5B, bottom left panel).[70] In contrast, neighboring nonexpressing cells within the same field retained strong TMRE fluorescence, supporting the absence of detectable bystander effects under these conditions. These results show that mitochondrial targeting of the photocatalyst enables a spatially restricted mitochondrial response to red-light irradiation. To evaluate single-cell spatiotemporal precision, a single Mito-HaloTag-expressing cell was selectively targeted using a 633 nm confocal FRAP module. Proximity-activated photocatalytic uncaging of DNP-Bpin triggered selective mitochondrial depolarization in the targeted cell (ROI 1), as evidenced by rapid dissipation of TMRE fluorescence (Figure 5C and Supplementary Movie S1). In contrast, the adjacent HaloTag-negative control cell (ROI 2), which was not labeled by CA-SiR, maintained a high TMRE signal, supporting spatially restricted actuation without detectable bystander toxicity.[71]

The Mito-Halo-SiR platform exhibited tunability, with mitochondrial depolarization increasing in a concentration-dependent manner. Increasing the concentration of DNP-Bpin from 10 to 100 $\mu$M resulted in progressively greater TMRE loss (Figure S30A). Meanwhile, mitochondrial expression of Halo-SiR combined with red-light irradiation maintained high cell viability (>95%) (Figure 5B, bottom middle panel), indicating that proximity-activated metabolic regulation can be achieved with minimal phototoxicity. Having established tunable activity and cytocompatibility, we next asked whether the subcellular location of photocatalysis influences biological outcome beyond the overall catalyst loading and irradiation conditions. To address this question, cells expressing whole-cell-Halo-SiR, which distributes throughout the cytosol and nucleus, were examined under identical catalyst loading and irradiation conditions.

Under identical catalyst loading and irradiation conditions, cells expressing whole-cell-Halo-SiR exhibited no significant loss of $\Delta\psi_m$ (Figure 5B, bottom right panel). This direct comparison demonstrates that mitochondrial localization of the photocatalyst is critical for efficient mitochondrial depolarization under these conditions, rather than catalyst expression alone being sufficient. The enhanced response is consistent with the importance of proximity-activated DNP generation at the mitochondrial membrane, where local drug concentration may facilitate metabolic uncoupling. Consistent with this conclusion, DNP-Bpin 9 (100 $\mu$M) produced no detectable TMRE loss in cells lacking the photocatalyst under red-light irradiation (Figure S30B). Meanwhile, partial recovery of Halo-SiR fluorescence was observed following local irradiation and an 8 min dark interval (Figure S30C). Together, these findings support the conclusion that the subcellular site of photocatalytic activation is a critical determinant of pharmacological outcome and demonstrate that genetically targeted red-light photocatalysis can enable proximity-activated metabolic regulation.

## Proximity-Activated Photocatalytic Pharmacology Enables Spatially Precise Epigenetic Regulation

Having established that the subcellular site of photocatalysis is a critical determinant of mitochondrial regulation under the tested conditions, we next asked whether the same principle extends to epigenetic signaling, where the spatial site of enzyme inhibition may likewise influence the biological outcome. Histone deacetylases (HDACs), which regulate chromatin architecture and gene expression, provide an ideal model for testing this hypothesis.[72,73] Existing approaches, including PROTACs and photoswitched inhibitors, often lack the subcellular precision required to selectively perturb nuclear HDAC activity without affecting the cytosolic pathways.[74,75] We therefore hypothesized that combining protein-controlled photochemical redirection with genetically encoded nuclear targeting could enable proximity-activated photocatalytic pharmacology, allowing HDAC inhibition to occur preferentially near the site of photocatalyst localization while reducing the exposure of the surrounding cytosol to the released inhibitor.

Downloaded from pubs.acs.org/acscii/article-pdf/doi/10.1021/acscentsci.6c01125/6907094/acscentsci.6c01125.pdf by SHANGHAI INST OF ORGANIC CHEMISTRY, Yiyun Chen on 04 November 2026


https://doi.org/10.1021/acscentsci.6c01125
ACS Cent. Sci. XXXX, XXX, XXX−XXX

To test this hypothesis, we paired a nuclear-localized Halo−SiR hybrid photocatalyst (NLS-Halo-SiR) with the boronate-caged clinical HDAC inhibitor Entinostat (MS-275-Bpin, **10**), which remains biologically inert until photocatalytically activated (Figure 6A). MS-275 is a C I-selective histone deacetylase (HDAC) inhibitor that potently inhibits HDAC1 and HDAC3, displays weaker activity toward HDAC2, and shows negligible activity against class II HDACs.[76] Because class I HDACs regulate transcriptional repression, chromatin compaction, cell-cycle progression, and apoptosis within the nucleus, nuclear-targeted photocatalytic release of MS-275 maximizes proximity-activated target occupancy and enzyme inhibition directly at the chromatin interface.

We first established that the caged HDAC inhibitor could be efficiently activated by red-light photocatalysis. In PBS buffer, irradiation of MS-275-Bpin **10** in the presence of 10 $\mu$M SiR for 30 min produced the active inhibitor MS-275 in 58% yield (Figure 6A; Figure S31). We next asked whether the released drug retained its expected biological activity. HDAC activity was quantified using the fluorogenic substrate Boc-Lys(Ac)-AMC, in which deacetylation by active HDACs liberates fluorescent AMC.[77] Prior to photocatalytic activation, the caged prodrug **10** remained completely inactive at concentrations up to 100 $\mu$M in HeLa nuclear extracts (Figure S32A). Following red-light activation, HDAC activity decreased to 42% of the control level (Figure S32B), whereas omission of the photocatalyst, prodrug, or light abolished the response (Figure S32C). These results establish MS-275-Bpin as a stable photocaged prodrug that can be activated with high fidelity, providing the molecular basis for proximity-activated HDAC regulation in living cells.

To determine whether proximity-activated photocatalysis could reprogram epigenetic signaling in living cells, we implemented the nuclear-targeted NLS-Halo-SiR hybrid photocatalyst and monitored histone H3 lysine 9 acetylation (H3K9ac), a canonical readout of HDAC inhibition (Figure 6B). The caged prodrug **10** alone produced no detectable change in basal H3K9 acetylation (Figure S33), confirming its biological inertness prior to photocatalytic activation. In contrast, 20 min of red-light irradiation in cells expressing NLS-Halo-SiR triggered a 2.2-fold increase in H3K9ac (Figure 6B, left panel). Importantly, the epigenetic response was readily tunable, with H3K9ac levels increasing progressively from 1.5- to 3.0-fold as the irradiation time was extended (Figure 6B, middle panel). These results demonstrate that the Halo-SiR platform enables precise temporal control over epigenetic regulation through light-directed photocatalytic drug activation.

Most importantly, nuclear-confined photocatalysis elicited a markedly enhanced 2.9-fold increase in H3K9 acetylation, substantially outperforming the 1.9-fold response produced by globally distributed catalysis despite an identical photon dose and catalyst loading (Figure 6B, right panel). This pronounced difference reveals a previously unrecognized spatial efficacy gap in optical pharmacology, demonstrating that pharmacological outcome depends not simply on the total amount of released drug but on where it is generated. By concentrating inhibitor release directly at the chromatin interface, nuclear-localized photocatalysis maximizes productive engagement with nuclear HDACs while minimizing diffusion-driven dilution throughout the cell. These findings establish subcellular proximity to the molecular target as a critical determinant of epigenetic reprogramming, a design principle that remains largely inaccessible to conventional diffusion-limited pharmacology.

Cytocompatibility analysis in HEK 293T cells first confirmed that targeted expression of the Halo-SiR hybrid photocatalyst, followed by red-light irradiation (130 mW cm$^{-2}$), maintained excellent cell viability (>95%), demonstrating the high biocompatibility of the platform (Figure 6C, left panel). We next evaluated whether proximity-activated photocatalysis could regulate endogenous HDAC activity in living cells. In cells expressing NLS-Halo-SiR, treatment with **10** (2 $\mu$M) followed by red-light irradiation produced a 24% reduction in HDAC activity, whereas control experiments lacking either the photocatalyst, prodrug, or light showed no measurable inhibition (Figure 6C, middle panel; Figure S34A,B).[77] These results confirm that HDAC inhibition is both spatially confined and strictly dependent on photocatalytic activation. We next asked whether this proximity-activated pharmacological response could be maintained under biologically relevant light attenuation. Importantly, efficient HDAC inhibition remained fully operational through a 1.5 mm tissue barrier, demonstrating that protein-controlled red-light photocatalysis sustains biological function under attenuated photon flux (Figure 6C, right panel). Consistent with the epigenetic analyses above, nuclear-localized catalysis produced stronger enzymatic inhibition than whole-cell-distributed catalysis (24% versus 17%; Figure S34C). These findings demonstrate that nuclear sequestration enhances pharmacological efficacy by concentrating photocatalytic drug release directly at its site of action while minimizing diffusion-driven dilution throughout the cytosol.

These findings establish proximity-activated photocatalytic pharmacology as a general strategy for spatially precise molecular regulation. By coupling protein microenvironment engineering with genetically encoded subcellular targeting, this approach demonstrates that the site of photocatalytic activation—not merely the total amount of released drug—can dictate biological outcome. More broadly, they demonstrate that engineering the protein microenvironment provides a general mechanism for redirecting photocatalytic reaction pathways, transforming it from a predominantly destructive modality into a programmable technology for high-fidelity molecular regulation in living systems.

## CONCLUSIONS

In summary, we establish protein-mediated photochemical redirection as a strategy for enabling proximity-activated red-light photocatalytic pharmacology. We developed a genetically encoded Halo−SiR protein−photocatalyst hybrid that enables near-quantitative bioorthogonal deboronative hydroxylation with high cellular compatibility. Structural and photophysical studies support a model in which the HaloTag scaffold stabilizes and confines the photoactive open zwitterionic SiR state while providing a distinct local reaction environment. This protein-mediated control is associated with preferential Type I photochemical reactivity, enhanced oxygen activation, and strongly suppressed singlet oxygen generation, thereby enabling efficient photocatalytic deboronative hydroxylation under biologically compatible conditions.

The resulting hybrid photocatalyst enables spatially localized regulation of cellular processes including mitochondrial function and epigenetic signaling. Nuclear-localized photocatalysis produced a 2.9-fold increase in H3K9 acetylation compared with 1.9-fold for nonlocalized activation under

Downloaded from pubs.acs.org/acscii/article-pdf/doi/10.1021/acscentsci.6c01125/6907094/acscentsci.6c01125.pdf by SHANGHAI INST OF ORGANIC CHEMISTRY, Yiyun Chen on 04 November 2026


https://doi.org/10.1021/acscentsci.6c01125
ACS Cent. Sci. XXXX, XXX, XXX−XXX

identical catalyst loading and irradiation conditions. This difference shows that the pharmacological outcome depends not only on the amount of drug released but also on the subcellular site of photocatalytic activation, highlighting catalyst localization as an important design parameter for optical pharmacology. Together with the spatially restricted mitochondrial response observed with Mito-Halo-SiR, these results demonstrate that the genetically programmed localization of photocatalysis can translate into proximity-activated biological regulation.

More broadly, this work demonstrates that protein scaffolds can provide an additional level of control over synthetic photocatalysts by stabilizing and confining their photoactive states while defining their local reaction environments and subcellular localizations. Recent advances have expanded the scope of red light photochemistry through biomarker-gated activation,[78] metal-coordinated photocatalysts,[79] diffusible SiR catalysts,[27] and direct BODIPY photocaging.[80] Complementing these approaches, our Halo-SiR platform combines protein-mediated control of the photoactive SiR state with genetically programmable subcellular targeting. This architecture provides a modular strategy for proximity-activated red light photocatalysis and spatially controlled optical pharmacology in living systems.

## ■ ASSOCIATED CONTENT

### Data Availability Statement

All relevant data are included in the manuscript and Supporting Information.

### Supporting Information

The Supporting Information is available free of charge at https://pubs.acs.org/doi/10.1021/acscentsci.6c01125.

NMR spectra of compounds **6** and **10**, as well as additional experimental details, materials, and methods (PDF)

Spatially confined mitochondrial depolarization induced by Mito-Halo−SiR photocatalysis (MP4)

Description of Supplementary Movie S1 (TXT)

## ■ AUTHOR INFORMATION


### Corresponding Authors

**Yiyun Chen** − *State Key Laboratory of Chemical Biology, Shanghai Institute of Organic Chemistry, University of Chinese Academy of Sciences, Chinese Academy of Sciences, Shanghai 200032, China; ShanghaiTech University, Shanghai 201210, China; School of Chemistry and Material Sciences, Hangzhou Institute for Advanced Study, University of Chinese Academy of Sciences, Hangzhou 310024, China;* orcid.org/0000-0003-0916-0994; Email: yiyunchen@sioc.ac.cn

**Yixin Zhang** − *State Key Laboratory of Chemical Biology, Shanghai Institute of Organic Chemistry, University of Chinese Academy of Sciences, Chinese Academy of Sciences, Shanghai 200032, China*; Email: zhangyixin@sioc.ac.cn

**Yi Zeng** − *Key Laboratory of Photochemical Conversion and Optoelectronic Materials, Technical Institute of Physics and Chemistry, Chinese Academy of Sciences, University of Chinese Academy of Sciences, Beijing 100190, China;* orcid.org/0000-0003-0694-1795; Email: zengyi@mail.ipc.ac.cn

### Authors

**Ru He** − *State Key Laboratory of Chemical Biology, Shanghai Institute of Organic Chemistry, University of Chinese Academy of Sciences, Chinese Academy of Sciences, Shanghai 200032, China; ShanghaiTech University, Shanghai 201210, China*

**Qihang Zhao** − *State Key Laboratory of Chemical Biology, Shanghai Institute of Organic Chemistry, University of Chinese Academy of Sciences, Chinese Academy of Sciences, Shanghai 200032, China*

**Zikang Chen** − *Key Laboratory of Photochemical Conversion and Optoelectronic Materials, Technical Institute of Physics and Chemistry, Chinese Academy of Sciences, University of Chinese Academy of Sciences, Beijing 100190, China*

**Xiuyu Wang** − *State Key Laboratory of Chemical Biology, Shanghai Institute of Organic Chemistry, University of Chinese Academy of Sciences, Chinese Academy of Sciences, Shanghai 200032, China; School of Chemistry and Material Sciences, Hangzhou Institute for Advanced Study, University of Chinese Academy of Sciences, Hangzhou 310024, China*

**Qiaoling Che** − *State Key Laboratory of Chemical Biology, Shanghai Institute of Organic Chemistry, University of Chinese Academy of Sciences, Chinese Academy of Sciences, Shanghai 200032, China; ShanghaiTech University, Shanghai 201210, China*

**Kaixing Zeng** − *State Key Laboratory of Chemical Biology, Shanghai Institute of Organic Chemistry, University of Chinese Academy of Sciences, Chinese Academy of Sciences, Shanghai 200032, China; ShanghaiTech University, Shanghai 201210, China*

Complete contact information is available at: https://pubs.acs.org/10.1021/acscentsci.6c01125


### Author Contributions

#R.H. and Q.Z. contributed equally to this work. R.H., Q.Z., and Y.C. designed the research and analyzed the data. R.H., Q.Z., X.W., Q.C., and K.Z. synthesized the probes and performed the experiments. Z.C. and Y.Z. conducted and analyzed the EPR and TA experiments. R.H., Q.Z., Y.Z., and Y.C. wrote the manuscript. All authors discussed the results and commented on the manuscript.

### Notes

Statistical information: A general statistical analysis was performed with a two-tailed Student's $t$ test (considered significant for $p < 0.05$) unless it was stated otherwise. Visualization of the final figures was done with Adobe Illustrator CS5.

The authors declare no competing financial interest.

## ■ ACKNOWLEDGMENTS

This research was supported by the National Natural Science Foundation of China (grants 22337005, 22277133), the Strategic Priority Research Program of the Chinese Academy of Sciences (XDB1060000), the Youth Innovation Promotion Association CAS (2023266), Lingang Laboratory Grant No. LGL-2617-01.

## ■ REFERENCES

(1) Fehrentz, T.; Schönberger, M.; Trauner, D. Optochemical Genetics. *Angew. Chem., Int. Ed.* **2011**, *50* (51), 12156−12182.

Downloaded from pubs.acs.org/acscii/article-pdf/doi/10.1021/acscentsci.6c01125/6907094/acscentsci.6c01125.pdf by SHANGHAI INST OF ORGANIC CHEMISTRY, Yiyun Chen on 04 November 2026

(2) Gautier, A.; Gauron, C.; Volovitch, M.; Bensimon, D.; Jullien, L.; Vriz, S. How to control proteins with light in living systems. *Nat. Chem. Biol.* **2014**, *10* (7), 533−541.
(3) Volarić, J.; Szymanski, W.; Simeth, N. A.; Feringa, B. L. Molecular photoswitches in aqueous environments. *Chem. Soc. Rev.* **2021**, *50* (22), 12377−12449.
(4) Charette, M.; Rosenblum, C.; Shade, O.; Deiters, A. Optogenetics with Atomic Precision−A Comprehensive Review of Optical Control of Protein Function through Genetic Code Expansion. *Chem. Rev.* **2025**, *125* (4), 1663−1717.
(5) Barr, J.; Cadoni, E.; Schellinck, S.; Laudadio, E.; Martins, J. C.; Madder, A. Locking up G-Quadruplexes with Light-Triggered Staples Leads to Increased Topological, Thermodynamic, and Metabolic Stability. *Angew. Chem., Int. Ed.* **2025**, *64* (9), No. e202420592.
(6) Pitruzzello, G. Seeing into deep tissue. *Nat. Photonics* **2023**, *17* (5), 376−377.
(7) Xiong, H.; Xu, Y.; Kim, B.; Rha, H.; Zhang, B.; Li, M.; Yang, G.-F.; Kim, J. S. Photo-controllable biochemistry: Exploiting the photocages in phototherapeutic window. *Chem.* **2023**, *9* (1), 29−64.
(8) Tsang, C. Y.; Zhang, Y. Nanomaterials for light-mediated therapeutics in deep tissue. *Chem. Soc. Rev.* **2024**, *53* (6), 2898−2931.
(9) Weinstain, R.; Slanina, T.; Kand, D.; Klán, P. Visible-to-NIR-Light Activated Release: From Small Molecules to Nanomaterials. *Chem. Rev.* **2020**, *120* (24), 13135−13272.
(10) He, G.; He, M.; Wang, R.; Li, X.; Hu, H.; Wang, D.; Wang, Z.; Lu, Y.; Xu, N.; Du, J.; Fan, J.; Peng, X.; Sun, W. A Near-Infrared Light-Activated Photocage Based on a Ruthenium Complex for Cancer Phototherapy. *Angew. Chem., Int. Ed.* **2023**, *62* (24), No. e202218768.
(11) Cabanero, D. C.; Rovis, T. Low-energy photoredox catalysis. *Nat. Rev. Chem.* **2025**, *9* (1), 28−45.
(12) Liang, X.; Qian, S.; Lou, Z.; Hu, R.; Hou, Y.; Chen, P. R.; Fan, X. Near Infrared Light-Triggered Photocatalytic Decaging for Remote-Controlled Spatiotemporal Activation in Living Mice. *Angew. Chem., Int. Ed.* **2023**, *62* (48), No. e202310920.
(13) Zhao, Z.; Li, J.; Yuan, W.; Cheng, D.; Ma, S.; Li, Y.-F.; Shi, Z.-J.; Hu, K. Nature-Inspired Photocatalytic Azo Bond Cleavage with Red Light. *J. Am. Chem. Soc.* **2024**, *146* (2), 1364−1373.
(14) Mato, M.; Fernández-González, X.; D'Avino, C.; Tomás-Gamasa, M.; Mascareñas, J. L. Bioorthogonal Synthetic Chemistry Enabled by Visible-Light Photocatalysis. *Angew. Chem., Int. Ed.* **2024**, *63* (47), No. e202413506.
(15) Buksh, B. F.; Knutson, S. D.; Oakley, J. V.; Bissonnette, N. B.; Oblinsky, D. G.; Schwoerer, M. P.; Seath, C. P.; Geri, J. B.; Rodriguez-Rivera, F. P.; Parker, D. L.; Scholes, G. D.; Ploss, A.; MacMillan, D. W. C. μMap-Red: Proximity Labeling by Red Light Photocatalysis. *J. Am. Chem. Soc.* **2022**, *144* (14), 6154−6162.
(16) Tay, N. E. S.; Ryu, K. A.; Weber, J. L.; Olow, A. K.; Cabanero, D. C.; Reichman, D. R.; Oslund, R. C.; Fadeyi, O. O.; Rovis, T. Targeted activation in localized protein environments via deep red photoredox catalysis. *Nat. Chem.* **2023**, *15* (1), 101−109.
(17) Di Mascio, P.; Martinez, G. R.; Miyamoto, S.; Ronsein, G. E.; Medeiros, M. H. G.; Cadet, J. Singlet Molecular Oxygen Reactions with Nucleic Acids, Lipids, and Proteins. *Chem. Rev.* **2019**, *119* (3), 2043−2086.
(18) Dolmans, D. E. J. G. J.; Fukumura, D.; Jain, R. K. Photodynamic therapy for cancer. *Nat. Rev. Cancer* **2003**, *3* (5), 380−387.
(19) Obaid, G.; Celli, J. P.; Broekgaarden, M.; Bulin, A.-L.; Uusimaa, P.; Pogue, B.; Hasan, T.; Huang, H.-C. Engineering photodynamics for treatment, priming and imaging. *Nat. Rev. Bioeng.* **2024**, *2* (9), 752−769.
(20) Deng, Z.; Li, H.; Chen, S.; Wang, N.; Liu, G.; Liu, D.; Ou, W.; Xu, F.; Wang, X.; Lei, D.; Lo, P.-C.; Li, Y. Y.; Lu, J.; Yang, M.; He, M.-L.; Zhu, G. Near-infrared-activated anticancer platinum(IV) complexes directly photooxidize biomolecules in an oxygen-independent manner. *Nat. Chem.* **2023**, *15* (7), 930−939.
(21) Liu, M.; Luo, Y.; Yan, J.; Xiong, X.; Xing, X.; Kim, J. S.; Zou, T. Photoactivation of Boronic Acid Prodrugs via a Phenyl Radical Mechanism: Iridium(III) Anticancer Complex as an Example. *J. Am. Chem. Soc.* **2023**, *145* (18), 10082−10091.
(22) Peng, W.; Zhou, T.; Hu, L.; Vankann, V.; Bohn, T.; Bopp, T.; Kuan, S. L.; Weil, T. Autonomous Activation of a Gated Chemiluminescent Photosensitizer Enables Targeted Photodynamic Therapy in Tumor Cells. *J. Am. Chem. Soc.* **2025**, *147* (31), 27822−27834.
(23) Lukinavičius, G.; Umezawa, K.; Olivier, N.; Honigmann, A.; Yang, G.; Plass, T.; Mueller, V.; Reymond, L.; Corrêa, I. R., Jr; Luo, Z.-G.; Schultz, C.; Lemke, E. A.; Heppenstall, P.; Eggeling, C.; Manley, S.; Johnsson, K. A near-infrared fluorophore for live-cell super-resolution microscopy of cellular proteins. *Nat. Chem.* **2013**, *5* (2), 132−139.
(24) Wang, C.; Zhang, H.; Zhang, T.; Zou, X.; Wang, H.; Rosenberger, J. E.; Vannam, R.; Trout, W. S.; Grimm, J. B.; Lavis, L. D.; Thorpe, C.; Jia, X.; Li, Z.; Fox, J. M. Enabling In Vivo Photocatalytic Activation of Rapid Bioorthogonal Chemistry by Repurposing Silicon-Rhodamine Fluorophores as Cytocompatible Far-Red Photocatalysts. *J. Am. Chem. Soc.* **2021**, *143* (28), 10793−10803.
(25) Jemas, A.; Xie, Y.; Pigga, J. E.; Caplan, J. L.; am Ende, C. W.; Fox, J. M. Catalytic Activation of Bioorthogonal Chemistry with Light (CABL) Enables Rapid, Spatiotemporally Controlled Labeling and No-Wash, Subcellular 3D-Patterning in Live Cells Using Long Wavelength Light. *J. Am. Chem. Soc.* **2022**, *144* (4), 1647−1662.
(26) Rosenberger, J. E.; Xie, Y.; Fang, Y.; Lyu, X.; Trout, W. S.; Dmitrenko, O.; Fox, J. M. Ligand-Directed Photocatalysts and Far-Red Light Enable Catalytic Bioorthogonal Uncaging inside Live Cells. *J. Am. Chem. Soc.* **2023**, *145* (11), 6067−6078.
(27) Yan, X.; Zhao, J.-H.; Wang, Q.; Wang, W.; Ding, Y.; Zhou, Y.; Chen, G.; Du, J.; Huang, W.; Chu, L. Silicon Rhodamine-Catalyzed Near-Infrared Light-Induced Photodecaging of Ortho-Nitrobenzyl Groups In Vitro and In Vivo. *J. Am. Chem. Soc.* **2025**, *147* (24), 20957−20966.
(28) Emmanuel, M. A.; Bender, S. G.; Bilodeau, C.; Carceller, J. M.; DeHovitz, J. S.; Fu, H.; Liu, Y.; Nicholls, B. T.; Ouyang, Y.; Page, C. G.; Qiao, T.; Raps, F. C.; Sorigué, D. R.; Sun, S.-Z.; Turek-Herman, J.; Ye, Y.; Rivas-Souchet, A.; Cao, J.; Hyster, T. K. Photobiocatalytic Strategies for Organic Synthesis. *Chem. Rev.* **2023**, *123* (9), 5459−5520.
(29) Kissman, E. N.; Sosa, M. B.; Millar, D. C.; Koleski, E. J.; Thevasundaram, K.; Chang, M. C. Y. Expanding chemistry through in vitro and in vivo biocatalysis. *Nature* **2024**, *631* (8019), 37−48.
(30) Huang, X.; Wang, B.; Wang, Y.; Jiang, G.; Feng, J.; Zhao, H. Photoenzymatic enantioselective intermolecular radical hydroalkylation. *Nature* **2020**, *584* (7819), 69−74.
(31) Zeng, S.; Liu, X.; Kafuti, Y. S.; Kim, H.; Wang, J.; Peng, X.; Li, H.; Yoon, J. Fluorescent dyes based on rhodamine derivatives for bioimaging and therapeutics: recent progress, challenges, and prospects. *Chem. Soc. Rev.* **2023**, *52* (16), 5607−5651.
(32) Wang, L.; Tran, M.; D'Este, E.; Roberti, J.; Koch, B.; Xue, L.; Johnsson, K. A general strategy to develop cell permeable and fluorogenic probes for multicolour nanoscopy. *Nat. Chem.* **2020**, *12* (2), 165−172.
(33) Deng, F.; Qiao, Q.; Li, J.; Yin, W.; Miao, L.; Liu, X.; Xu, Z. Multiple Factors Regulate the Spirocyclization Equilibrium of Si-Rhodamines. *J. Phys. Chem. B* **2020**, *124* (34), 7467−7474.
(34) Mashaghi, A.; Kramer, G.; Bechtluft, P.; Zachmann-Brand, B.; Driessen, A. J. M.; Bukau, B.; Tans, S. J. Reshaping of the conformational search of a protein by the chaperone trigger factor. *Nature* **2013**, *500* (7460), 98−101.
(35) Santana, A. G.; Robinson, K.; Vickers, C.; Deen, M. C.; Chen, H.-M.; Zhou, S.; Dai, B.; Fuller, M.; Boraston, A. B.; Vocadlo, D. J.; Clarke, L. A.; Withers, S. G. Pharmacological Chaperones for GCase that Switch Conformation with pH Enhance Enzyme Levels in Gaucher Animal Models. *Angew. Chem., Int. Ed.* **2022**, *61* (38), No. e202207974.

Downloaded from pubs.acs.org/acscii/article-pdf/doi/10.1021/acscentsci.6c01125/6907094/acscentsci.6c01125.pdf by SHANGHAI INST OF ORGANIC CHEMISTRY, Yiyun Chen on 04 November 2026


https://doi.org/10.1021/acscentsci.6c01125
ACS Cent. Sci. XXXX, XXX, XXX−XXX

(36) Sletten, E. M.; Bertozzi, C. R. Bioorthogonal Chemistry: Fishing for Selectivity in a Sea of Functionality. *Angew. Chem., Int. Ed.* **2009**, *48* (38), 6974−6998.
(37) Jang, S.-Y.; Murale, D. P.; Kim, A. D.; Lee, J.-S. Recent Developments in Metal-Catalyzed Bio-orthogonal Reactions for Biomolecule Tagging. *ChemBioChem.* **2019**, *20* (12), 1498−1507.
(38) Li, J.; Kong, H.; Zhu, C.; Zhang, Y. Photo-controllable bioorthogonal chemistry for spatiotemporal control of bio-targets in living systems. *Chem. Sci.* **2020**, *11* (13), 3390−3396.
(39) Kumar, G. S.; Lin, Q. Light-Triggered Click Chemistry. *Chem. Rev.* **2021**, *121* (12), 6991−7031.
(40) Finn, M. G.; Kolb, H. C.; Sharpless, K. B. Click chemistry connections for functional discovery. *Nat. Synth.* **2022**, *1* (1), 8−10.
(41) Li, S.; Pang, J.; Sun, Y.; Zhang, Y.; Long, Y.-Q. Conditional Relay Activation of Theranostic Prodrug by Pretargeting Bioorthogonal Trigger and Fluorescence-Guided Visible Light Irradiation. *Angew. Chem., Int. Ed.* **2025**, *64* (12), No. e202422023.
(42) Hall, D. G. Structure, Properties, and Preparation of Boronic Acid Derivatives. In *Boronic Acids: Preparation and Applications in Organic Synthesis, Medicine and Materials*, Hall, D. G., Ed.; Wiley-VCH: 2011; pp 1−133. DOI: 10.1002/9783527639328.ch1.
(43) Lippert, A. R.; Van de Bittner, G. C.; Chang, C. J. Boronate Oxidation as a Bioorthogonal Reaction Approach for Studying the Chemistry of Hydrogen Peroxide in Living Systems. *Acc. Chem. Res.* **2011**, *44* (9), 793−804.
(44) Grams, R. J.; Santos, W. L.; Scorei, I. R.; Abad-García, A.; Rosenblum, C. A.; Bita, A.; Cerecetto, H.; Viñas, C.; Soriano-Ursúa, M. A. The Rise of Boron-Containing Compounds: Advancements in Synthesis, Medicinal Chemistry, and Emerging Pharmacology. *Chem. Rev.* **2024**, *124* (5), 2441−2511.
(45) Chung, C. Y.; Timblin, G. A.; Saijo, K.; Chang, C. J. Versatile Histochemical Approach to Detection of Hydrogen Peroxide in Cells and Tissues Based on Puromycin Staining. *J. Am. Chem. Soc.* **2018**, *140* (19), 6109−6121.
(46) Zou, Y.-Q.; Chen, J.-R.; Liu, X.-P.; Lu, L.-Q.; Davis, R. L.; Jørgensen, K. A.; Xiao, W.-J. Highly Efficient Aerobic Oxidative Hydroxylation of Arylboronic Acids: Photoredox Catalysis Using Visible Light. *Angew. Chem., Int. Ed.* **2012**, *51* (3), 784−788.
(47) Wang, H.; Li, W.-G.; Zeng, K.; Wu, Y.-J.; Zhang, Y.; Xu, T.-L.; Chen, Y. Photocatalysis Enables Visible-Light Uncaging of Bioactive Molecules in Live Cells. *Angew. Chem., Int. Ed.* **2019**, *58* (2), 561−565.
(48) Zeng, K.; Jiao, Z.-H.; Jiang, Q.; He, R.; Zhang, Y.; Li, W.-G.; Xu, T.-L.; Chen, Y. Genetically Encoded Photocatalysis Enables Spatially Restricted Optochemical Modulation of Neurons in Live Mice. *ACS Central Science* **2024**, *10* (1), 163−175.
(49) Che, Q.; He, R.; Zhang, Y.; Zhang, H.; Zeng, K.; Chen, Y. Miniature Photoenzyme Enables Organelle-Specific Cellular Control via Deboronative Hydroxylation. *Angew. Chem., Int. Ed.* **2025**, *64* (51), No. e15137.
(50) Zhang, H.; Wang, X.; Xu, T.; Chen, Y. Proximity-Activated Photocatalytic Pharmacology: From Subcellular Compartments to Neural Circuits. *Acc. Chem. Res.* **2026**, DOI: 10.1021/acs.accounts.6c00470.
(51) Torra, J.; Lafaye, C.; Signor, L.; Aumonier, S.; Flors, C.; Shu, X.; Nonell, S.; Gotthard, G.; Royant, A. Tailing miniSOG: structural bases of the complex photophysics of a flavin-binding singlet oxygen photosensitizing protein. *Sci. Rep.* **2019**, *9* (1), 2428.
(52) Porzberg, N.; Gries, K.; Johnsson, K. Exploiting Covalent Chemical Labeling with Self-Labeling Proteins. *Annu. Rev. Biochem.* **2025**, *94* (1), 29−58.
(53) Zeng, K.; Han, L.; Chen, Y. Endogenous Proteins Modulation in Live Cells with Small Molecules and Light. *ChemBioChem.* **2022**, *23* (21), No. e202200244.
(54) Absorption-normalized benchmarking at 635 nm was also performed to account for differences in chromophore absorption. SiR showed high conversion under 635 nm irradiation, whereas several dyes with comparable red-light absorption also exhibited substantial activity after normalization (Figure S2).
(55) Kim, J.; Xu, Y.; Lim, J. H.; Lee, J. Y.; Li, M.; Fox, J. M.; Vendrell, M.; Kim, J. S. Bioorthogonal Activation of Deep Red Photoredox Catalysis Inducing Pyroptosis. *J. Am. Chem. Soc.* **2025**, *147* (1), 701−712.
(56) Pitre, S. P.; McTiernan, C. D.; Ismaili, H.; Scaiano, J. C. Mechanistic Insights and Kinetic Analysis for the Oxidative Hydroxylation of Arylboronic Acids by Visible Light Photoredox Catalysis: A Metal-Free Alternative. *J. Am. Chem. Soc.* **2013**, *135* (36), 13286−13289.
(57) Xiao, L.; Gu, C.; Xiang, Y. Orthogonal Activation of RNA-Cleaving DNAzymes in Live Cells by Reactive Oxygen Species. *Angew. Chem., Int. Ed.* **2019**, *58* (40), 14167−14172.
(58) Srikun, D.; Albers, A. E.; Chang, C. J. A dendrimer-based platform for simultaneous dual fluorescence imaging of hydrogen peroxide and pH gradients produced in living cells. *Chem. Sci.* **2011**, *2* (6), 1156−1165.
(59) Jiao, F.; Braitbard, M.; Yu, C.; Shor, B.; Wulff, B.-E.; Schneidman-Duhovny, D.; Huang, L. Cysteine-enabled cleavability to advance cross-linking mass spectrometry for global analysis of endogenous protein-protein interactions. *Nat. Commun.* **2025**, *16* (1), 11093.
(60) Los, G. V.; Encell, L. P.; McDougall, M. G.; Hartzell, D. D.; Karassina, N.; Zimprich, C.; Wood, M. G.; Learish, R.; Ohana, R. F.; Urh, M.; Simpson, D.; Mendez, J.; Zimmerman, K.; Otto, P.; Vidugiris, G.; Zhu, J.; Darzins, A.; Klaubert, D. H.; Bulleit, R. F.; Wood, K. V. HaloTag: A Novel Protein Labeling Technology for Cell Imaging and Protein Analysis. *ACS Chem. Biol.* **2008**, 3 (6), 373−382.
(61) Lardon, N.; Wang, L.; Tschanz, A.; Hoess, P.; Tran, M.; D'Este, E.; Ries, J.; Johnsson, K. Systematic Tuning of Rhodamine Spirocyclization for Super-resolution Microscopy. *J. Am. Chem. Soc.* **2021**, *143* (36), 14592−14600.
(62) Erdmann, R. S.; Baguley, S. W.; Richens, J. H.; Wissner, R. F.; Xi, Z.; Allgeyer, E. S.; Zhong, S.; Thompson, A. D.; Lowe, N.; Butler, R.; Bewersdorf, J.; Rothman, J. E.; St Johnston, D.; Schepartz, A.; Toomre, D. Labeling Strategies Matter for Super-Resolution Microscopy: A Comparison between HaloTags and SNAP-tags. *Cell Chem. Biol.* **2019**, *26* (4), 584−592.
(63) The HaloTag−SiR model was constructed using the HaloTag−TMR crystal structure (PDB 6ZVY) as a template and retains the experimentally resolved Asp106 anchoring site and linker trajectory. Because the model represents a static structure, it does not establish the relative thermodynamic stability of the open and closed SiR states.
(64) Under low catalyst loading (0.1 $\mu$M Halo−SiR; 200 $\mu$M substrate), the maximum observed product-based turnover number reached approximately 768 within 70 min (Figure S18). The high catalytic turnover prompted us to test the residual activity of a preirradiated sample. After 300 min of preirradiation, Halo-SiR fluorescence decreased to approximately 43% of the unbleached control; subsequent BA-Bpin conversion decreased from 36.1% to 26.8%, corresponding to 74.2% retained activity (Figure S19).
(65) A carbon-centered radical signal attributable to the $NAD^{\bullet}$ radical generated during NADH oxidation was also observed (Figure S21F).
(66) Owing to its slow transmembrane diffusion kinetics and the rapid time scale of the washing protocol (three consecutive 2 min wash cycles), the liberated AMC fluorophore is efficiently retained within the intracellular compartment during postirradiation processing and is further stabilized by paraformaldehyde (PFA) fixation during subsequent slide preparation. This spatial retention and the absence of significant passive efflux were rigorously validated via both microplate reader quantification and live-cell inverted fluorescence microscopy (Figure S25).
(67) Li, Y.; Liu, G.; Cheng, S.; Zhang, J.; Yao, X.; Xie, X.; Xu, C.; Tang, Y.; Wang, X.; Tang, B. Cellular Redox Regulation and Fluorescence Imaging. *Chem. Rev.* **2025**, *125* (16), 7725−7810.
(68) Kang, Y.; Chen, L. Structural basis for the binding of DNP and purine nucleotides onto UCP1. *Nature* **2023**, *620* (7972), 226−231.

Downloaded from pubs.acs.org/acscii/article-pdf/doi/10.1021/acscentsci.6c01125/6907094/acscentsci.6c01125.pdf by SHANGHAI INST OF ORGANIC CHEMISTRY, Yiyun Chen on 04 November 2026

(69) Shrestha, R.; Johnson, E.; Byrne, F. L. Exploring the therapeutic potential of mitochondrial uncouplers in cancer. *Mol. Metab.* **2021**, *51* (1), 101222.
(70) The sustained mitochondrial uncoupling activity observed postwashing is consistent with previous literature.[48,49] This persistence likely stems from the slow trans-membrane equilibration kinetics of localized DNP; prior transport assays demonstrate that short-term direct incubation with the free compound is insufficient to fully dissipate $\Delta\psi m$.
(71) Upon further extending the duration of light exposure, adjacent cells remained near baseline initially, with delayed responses only after prolonged incubation (Figure S29).
(72) Haberland, M.; Montgomery, R. L.; Olson, E. N. The many roles of histone deacetylases in development and physiology: implications for disease and therapy. *Nat. Rev. Genet.* **2009**, *10* (1), 32−42.
(73) Cavalli, G.; Heard, E. Advances in epigenetics link genetics to the environment and disease. *Nature* **2019**, *571* (7766), 489−499.
(74) Reis, S. A.; Ghosh, B.; Hendricks, J. A.; Szantai-Kis, D. M.; Törk, L.; Ross, K. N.; Lamb, J.; Read-Button, W.; Zheng, B.; Wang, H.; Salthouse, C.; Haggarty, S. J.; Mazitschek, R. Light-controlled modulation of gene expression by chemical optoepigenetic probes. *Nat. Chem. Biol.* **2016**, *12* (5), 317−323.
(75) Smalley, J. P.; Adams, G. E.; Millard, C. J.; Song, Y.; Norris, J. K. S.; Schwabe, J. W. R.; Cowley, S. M.; Hodgkinson, J. T. PROTAC-mediated degradation of class I histone deacetylase enzymes in corepressor complexes. *Chem. Commun.* **2020**, *56* (32), 4476−4479.
(76) Khan, N.; Jeffers, M.; Kumar, S.; Hackett, C.; Boldog, F.; Khramtsov, N.; Qian, X.; Mills, E.; Berghs, S. C.; Carey, N.; Finn, P. W.; Collins, L. S.; Tumber, A.; Ritchie, J.; Jensen, P. B.; Lichenstein, H. S.; Sehested, M. Determination of the class and isoform selectivity of small-molecule histone deacetylase inhibitors. *Biochem. J.* **2008**, *409* (2), 581−589.
(77) Krieger, V.; Hamacher, A.; Gertzen, C. G. W.; Senger, J.; Zwinderman, M. R. H.; Marek, M.; Romier, C.; Dekker, F. J.; Kurz, T.; Jung, M.; Gohlke, H.; Kassack, M. U.; Hansen, F. K. Design, Multicomponent Synthesis, and Anticancer Activity of a Focused Histone Deacetylase (HDAC) Inhibitor Library with Peptoid-Based Cap Groups. *J. Med. Chem.* **2017**, *60* (13), 5493−5506.
(78) Tong, G.; Li, C.; Zhou, Q.; Wang, F.; He, W.; Xiong, E.; Su, L.; Yang, S.; Liu, G.; Yang, R. Biomarker-Gated Photocatalysis Uncaging in Live System. *Angew. Chem., Int. Ed.* **2026**, *65* (4), No. e15936.
(79) Wu, C.; Wei, Z.; Li, C.; Yang, S.; Liu, G.; Yang, R. Bio-Photo Dual Action of Intracellular Radical Polymerization. *J. Am. Chem. Soc.* **2025**, *147* (39), 35604−35615.
(80) Li, H.; Li, Q.; Guo, L.; Guo, X.; Zhang, Q.; Wang, Z.; Wu, Q.; Wang, S.; Jiao, L.; Hao, E. Modular One-Pot Access to Boron-Carboxylated Dipyrromethene Dyes as Visible-Light and Two-Photon Activatable Photocages. *J. Am. Chem. Soc.* **2025**, *147* (35), 31900−31910.

Downloaded from pubs.acs.org/acscii/article-pdf/doi/10.1021/acscentsci.6c01125/6907094/acscentsci.6c01125.pdf by SHANGHAI INST OF ORGANIC CHEMISTRY, Yiyun Chen on 04 November 2026



https://doi.org/10.1021/acscentsci.6c01125
*ACS Cent. Sci.* XXXX, XXX, XXX−XXX